The Cryosphere, 19, 5095–5109, 2025 https://doi.org/10.5194/tc-19-5095-2025 © Author(s) 2025. This work is distributed under the Creative Commons Attribution 4.0 License.





# Folding due to anisotropy in ice, from drill-core-scale cloudy bands to km-scale internal reflection horizons

Paul D. Bons $^{1,2}$ , Yuanbang Hu $^{1,3}$ , M.-Gema Llorens $^4$ , Steven Franke $^1$ , Nicolas Stoll $^{5,6}$ , Ilka Weikusat $^{1,5}$ , Julien Westhoff $^7$ , and Yu Zhang $^1$ 

Correspondence: Paul D. Bons (paul.bons@uni-tuebingen.de)

Received: 4 December 2024 – Discussion started: 27 January 2025

Revised: 16 July 2025 - Accepted: 12 August 2025 - Published: 27 October 2025

Abstract. Upright folds in ice sheets are observed on the cm scale in cloudy bands in drill cores and on the km scale in radargrams. We address the question of the folding mechanism for these folds by analysing the power spectra of fold trains to obtain the amplitude as a function of wavelength signal. Classical Biot-type buckle folds due to a rheological contrast between layers develop a characteristic wavelength, visible as a peak in the power spectrum. Power spectra of ice folds, however, follow a power law, with a steady increase in amplitude with wavelength. Such a power spectrum is also observed in a folded, highly anisotropic biotite schist and in a numerical simulation of the deformation of ice Ih with a strong alignment of the basal planes parallel to the shortening direction. This suggests that the folds observed in ice are primarily due to the strong mechanical anisotropy of ice, which tends to have a strong lattice preferred orientation due to icesheet flow.

## 1 Introduction

Folds are observed on all scales in glaciers and ice sheets. Large-scale folds (100–1000 m scale) are observed via internal reflection horizons (IRHs) in radargrams (Wolovick et al., 2014; Bell et al., 2014; Panton and Karlsson, 2015; Leysinger-Vieli et al., 2018; NEEM community members,

2013; Bons et al., 2016; Franke et al., 2022a, 2023; Jansen et al., 2024) and in satellite images of the ice surface in West Greenland. Folds on the intermediate scale ( $\sim$  m scale) are common in glaciers (Hudleston, 2015) but more difficult to observe in ice sheets because of the snow cover. Small-scale folds (< 1 cm) in ice cores are visible as undulated "cloudy bands", thin layers of elevated impurity concentration mainly occurring in glacial periods (Thorsteinsson, 1996; Alley et al., 1997; Svensson et al., 2005; Faria et al., 2010; Fitzpatrick et al., 2014; Jansen et al., 2016; Weikusat et al., 2017; Stoll et al., 2023). These folds are the main topic of this paper, using examples from the East Greenland Ice-core Project (EGRIP) drill core (Westhoff et al., 2021, Fig. 1), which provided novel insights into the crystal orientation inside an ice stream (Stoll et al., 2025), i.e. the Northeast Greenland Ice Stream (NEGIS). Cloudy bands made visible in dark-field macroscopy in EGRIP ice have already been observed in ice originating from the Younger Dryas at 1257 m depth (Bohleber et al., 2023) and are a recurring stratigraphic feature from a depth of 1375 m (Westhoff et al., 2021; Stoll et al., 2023). Chemical data from these bands show elevated impurity concentration and more insoluble particles than in the surrounding layers (Bohleber et al., 2023; Stoll et al., 2023). Stoll et al. (2023) define different cloudy band types and discuss their formation, but little is known about the folding mechanism of these bands that are observed below 1375 m at EGRIP. Folds

<sup>&</sup>lt;sup>1</sup>Department of Geosciences, Tübingen University, Tübingen, Germany

<sup>&</sup>lt;sup>2</sup>China University of Geosciences (Beijing), Beijing, China

<sup>&</sup>lt;sup>3</sup>Center for High Pressure Science and Technology Advanced Research, Beijing, China

<sup>&</sup>lt;sup>4</sup>Geosciences Barcelona GEO3BCN-CSIC, Barcelona, Spain

<sup>&</sup>lt;sup>5</sup>Alfred Wegener Institute, Helmholtz Centre for Polar and Marine Research, Bremerhaven, Germany

<sup>&</sup>lt;sup>6</sup>Department of Environmental Sciences, Informatics and Statistics, Ca'Foscari University of Venice, Venice, Italy

<sup>&</sup>lt;sup>7</sup>Niels Bohr Institute, University of Copenhagen, Copenhagen, Denmark

are not always observed below this depth, which can be explained by the orientation of the drill-core section relative to the fold axis. Only sections at a large angle relative to the fold axis will reveal folds in the cloudy bands (Fig. 4 in Westhoff et al., 2021).

Nabavi and Fossen (2021) define folds as "curviplanar structures that form by transformation of any tectonic or primary foliation into curved geometries through a non-linear transformation". In geology, "foliation" is used to denote any pervasive planar structure in a rock (which includes ice). The primary foliation in glaciers and ice sheets is the original layering formed by the deposition of snow layers on the surface. Other foliations can, for example, be healed fractures or fractures filled with frozen water (Hudleston, 2015). Numerous causes for folding in ice sheets have been proposed. Variations in bedrock elevation (Krabbendam, 2016), variable bedrock sliding (Wolovick et al., 2014), and basal melting or freeze-on (Leysinger-Vieli et al., 2018) have been proposed to explain large-scale folds of the original stratigraphy. Such external causes for folding cannot apply to small-tomedium-scale folds that are observed throughout the column of the ice sheet well above the ice-bedrock interface. These folds must, therefore, be the result of an internal response to layer-parallel shortening (NEEM community members, 2013; Hudleston, 2015; Bons et al., 2016; Jansen et al., 2016; Zhang et al., 2024).

A volume of a mechanically homogeneous and isotropic material will not produce folds when subject to deformation, as the material would only thicken without experiencing localized strain. Folds can form when the material has a mechanical layering that forms a "composite anisotropy" and/or when it is "intrinsically anisotropic", for example, due to a crystallographic preferred orientation (CPO) (Griera et al., 2013; Nabavi and Fossen, 2021; Hansen et al., 2021). The latter is often the case in ice because ice normally deforms by dislocation creep (Glen, 1955; Weertman, 1983) that results in a CPO that aligns the easy-glide basal planes in certain preferred orientations, typically perpendicular to the maximum finite shortening direction (Duval et al., 1983; Budd and Jacka, 1989; Faria et al., 2014; Llorens et al., 2017). In both cases, the application of a differential stress will normally lead to a heterogenous deformation field, which implies that originally straight planar surfaces get distorted: folds develop. Here, we will show, based on fold theory and numerical simulations, that folds observed in cloudy bands in the EGRIP drill core primarily result from an intrinsic anisotropy due to the CPO and not from rheological differences between the individual cloudy bands.

## 2 Basic fold terminology and theory

For detailed reviews of fold geometry and terminology, the reader is referred to the textbooks of Ramsay and Huber (1987) and Twiss and Moores (2007) or to the extensive review by Nabavi and Fossen (2021), which also provides an

overview of fold theory. Here, we provide only a summary of the relevant terminology and theory based on the above publications, unless otherwise referenced.

Most fold trains roughly resemble a sinusoidal wave function (Fig. 2a). One individual fold consists of two limbs that meet at the fold hinge – the line of maximum curvature. When the fold hinges diverge downwards, the fold is termed an "antiform"; otherwise, it is a "synform". Antiforms and synforms join at the inflection points in the fold limbs where the direction of curvature changes sign. The terms "anticline" and "syncline" are reserved for folds in a stratigraphic sequence and, therefore, apply to folds observed in radargrams or cloudy bands, as these are assumed to represent sedimentary snow layers. Folds can have shapes that range from rectangular boxes, semi-ellipses, parabolas, and sine waves to chevron or kink folds (Nabavi and Fossen, 2021). Box folds have 2-fold hinges per fold, but the authors are unaware of any box folds reported in ice. Ideal chevron or kink folds have straight limbs and highly concentrated curvature in the hinges. Such folds were described in a drilled ice core by Jansen et al. (2016). As most folds resemble a sine wave, the term "wavelength" ( $\lambda$ ) is one metric used to describe the length scale of folds. It is defined as double the distance between inflection points in the directions of the fold train (Fig. 2a). Accordingly, the "amplitude" (A) is defined as half the distance between the average antiformal and synformal hinge lines, measured in the direction perpendicular to the fold train. Folds can, however, have multiple wavelengths (Fig. 2b), in which case defining the amplitude becomes difficult. The "arc length" is the length of a line along the fold trace. The relative arc length ratio is the ratio of the arc length and the length of a straight line along the fold trace. The arc length is the same as the initial length if a layer only folds and does not become thicker or thinner during folding.

Folds may form when a composite material consisting of layers with different rheology is shortened parallel to the layers. The reason for this "buckle folding" is that it is energetically more favourable to accommodate part of the shortening by bending the stronger layers at intervals (the fold hinges) and rotating the sections in between (the fold limbs). The weaker layers in between need to accommodate this deformation by deforming at a higher rate. Biot (1957) first developed the theory that the final fold wavelength is a function of the amplification rate of an infinite range of wavelengths of initial perturbations in the original layer. The basic idea is that the final wavelength is the one with the highest amplification rate. For a single layer with thickness H and linear viscosity  $\eta_{\rm II}$  embedded in an infinite matrix with viscosity  $\eta_{\rm m}$ , he derived for the dominant wavelength  $\lambda_{\rm d}$  the following:

$$\lambda_{\rm d} = 2\pi H \left(\frac{\eta_{\rm l}}{6\eta_{\rm m}}\right)^{1/3}.\tag{1}$$

For a certain  $\eta_1/\eta_m$  ratio, the dominant wavelength is proportional to the layer thickness, which explains why the folds

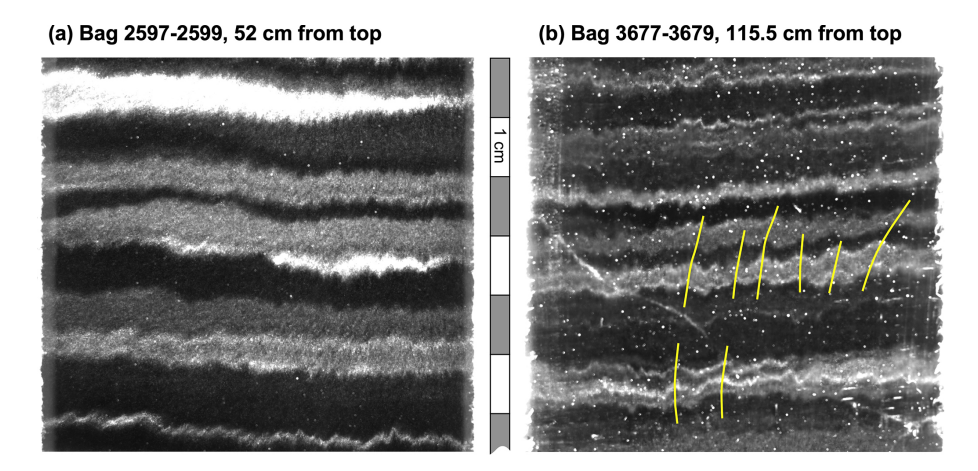


**Figure 1.** Two visual stratigraphy line scan examples of folded cloudy bands in the EGRIP drill core from a depth of **(a)** 1427.8 m and **(b)** 2017.45 m. Cloudy bands vary in thickness from about 1 to more than 10 mm. Eight axial planes are drawn as yellow lines in **(b)**. These show that the folds are upright or moderately inclined. The folds are disharmonic, as axial planes cannot be traced for over more than a few times the fold wavelength at most.

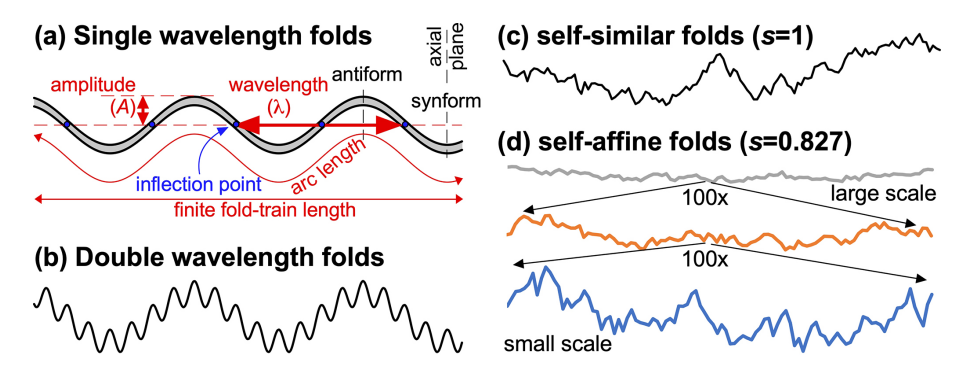


**Figure 2.** Fold shape and terminology. (a) Basic fold with a single wavelength. The arc length is the length of the fold train measured along the fold, while the finite length is the distance between the two ends of the fold train. (b) Fold composed of the superposition of two sine waves with different wavelengths and amplitudes. (c) Self-similar fold train in which the amplitude of folds is a linear function of the wavelength (s = 1 in Eq. 2). The artificial fold train is sampled every 0.5 mm if the whole fold train is 65 mm, comparable to the length of fold trains analysed in the EGRIP drill core. (d) Example of self-affine folds, where the amplitude/wavelength ratio systematically decreases with increasing scale (the variable s is defined in Eq. 2).

have varying wavelengths in the folded aplite dyke shown in Fig. 3a.

Since Biot's pioneering work, many authors have extended and refined his theory for multi-layers, elasticity, slip or no slip between layers, and non-linear (power-law) rheologies (see Table 2 in Schmalholz and Mancktelow, 2016). All these theories have in common that when the rheological difference between layers approaches zero, the dominant wavelength reduces to approximately the layer thickness. Wavelengths smaller than the layer thickness cannot be explained by Biot-type buckle-fold theory for layers with different rheological properties. It should also be noted that the fold amplification rate decreases with decreasing rheological contrasts (Llorens, 2019) in isotropic materials. This means that while relatively short wavelengths are possible at low rheo-

logical contrast between layers, one would not see the folds because their amplitude would be too small.

Relatively little work has been done on folding due to an intrinsic anisotropy, for example, the alignment of easy-glide basal planes in ice or aligned micas in a schist (Cobbold et al., 1971). Biot-type buckle-fold theory cannot be simply applied to predict a dominant wavelength, as there is no layer thickness to provide a length scale. Without a length scale in the system, folds of all wavelengths should amplify at the same rate. Instead of folds with a dominant wavelength, one would expect folds where the amplitude of each wavelength is proportional to that wavelength (Fig. 2c). In that case, we get

$$A_{(\lambda)} = \lambda_0 \cdot \lambda^s, \tag{2}$$

with  $\lambda_0$  being a proportionality constant and s the scaling variable. When s = 1, the folds are self-similar, meaning that

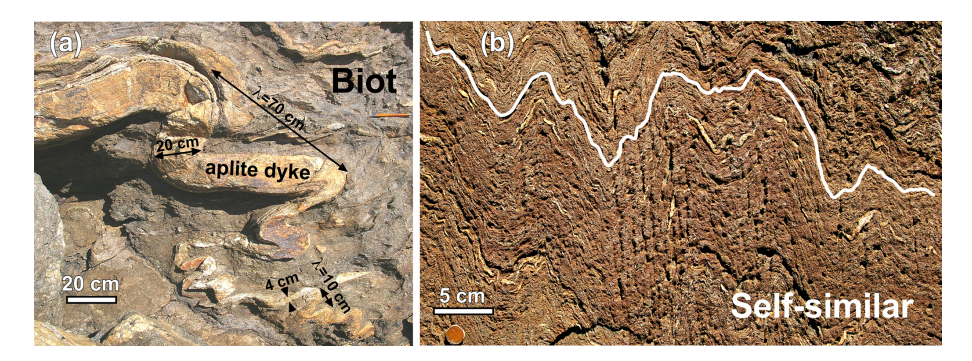


**Figure 3.** Examples of folds in rocks from Cap de Creus, northeast Catalonia, Spain. (a) Biot-type folding of a strong aplite dyke in a weaker granodiorite matrix. The example clearly shows the positive correlation between the thickness of the dyke and wavelength, which both decrease from the top left to the bottom right (Punta Fallarons; N42°20′25″, E3°15′48″). (b) Folded highly anisotropic biotite schist with thin quartz veins showing harmonic multi-wavelength folds. The hand-drawn white line was used for the analysis shown in Fig. 7b (Puig de Culip; N42°19′19″, E3°18′12″). Both photographs by Paul Bons.

folds at all scales look similar because the scaling of the amplitude and wavelength is identical (Fig. 2c). When s < 1, large folds have relatively smaller amplitudes than small folds (Fig. 2d). When the scaling of amplitudes and wavelengths is not identical, the folds are self-affine.

The above shows that the fold-amplitude function  $A_{(\lambda)}$  can be used to determine whether folds are due to Biottype buckling or due to shortening of an intrinsic mechanical anisotropy. Below, we apply Fourier transforms to the traces of folded cloudy bands and large-scale folds at EGRIP, a folded biotite schist, and numerically generated folds. The resulting fold-amplitude functions show that the cloudy-band folds are self-similar ( $s \approx 1$  in Eq. 2) and therefore due to the intrinsic mechanical anisotropy in the ice.

## 3 Materials and methods

#### 3.1 Materials

Ice Ih is mechanically comparable to highly anisotropic micas in metamorphic schists due to the alignment of platy mica grains into a foliation. Micas also deform most easily along their basal planes (Finch et al., 2020). Metamorphic schists at Cap de Creus, NE Catalonia, Spain, show folding of the foliation that happened during the Palaeozoic Variscan Orogeny (Druguet et al., 1997; Bons et al., 2004). The mechanical anisotropy of the foliated rock is thought to play a dominant role in the deformation of these rocks (Carreras et al., 2013; de Riese et al., 2019). We therefore use one outcrop as an example of folding of a strongly anisotropic rock in which layering is absent (Fig. 3b).

The East Greenland Ice-core Project (EGRIP) is a deep drilling project located in the middle of NEGIS at 75°37.820 N and 35°59.556 W. Visual stratigraphy line scans of the drill core reveal cloudy bands by imaging a polished slab of the core in dark-field macroscopy. When the section of the core is suitably oriented rela-

tive to the flow direction, these cloudy bands show folds (Fig. 4 in Westhoff et al., 2021). We used (Fig. 4) line-scan images 2597\_1\_32mm.bmp, 3128\_1\_32mm.bmp, and 23677\_1\_32mm.bmp (Weikusat et al., 2020), each representing three 55 cm bags, to make a core length of 165 cm in each image. The depth of the top of the three images is 1427.8, 1719.85, and 2021.8 m, respectively. We refer to these images by the number of their top bag, and depths of individual cloudy bands are given in cm from the top of the image.

Cloudy bands are visible only in drill cores with a width of  $<10\,\mathrm{cm}$ . Much larger-scale folds are observed in ice by means of radar data. We use high-resolution radar data from the EGRIP-NOR-2018 survey (Franke et al., 2022b) from the onset region of NEGIS. The radar data were acquired in May 2018 with the AWI's (Alfred Wegener Institute Helmholtz Centre for Polar and Marine Research) airborne multichannel ultra-wideband (UWB) radar and have a horizontal resolution of  $\sim 15\,\mathrm{m}$  and vertical resolution of 4.31 m. The radar-grams used here are centred at the EGRIP drill site and run perpendicular to the ice flow (Fig. 5).

# 3.2 Methods

#### 3.2.1 Numerical modelling

We use the full-field viscoplastic fast Fourier transform (VPFFT) crystal plasticity code (Lebensohn, 2001; Lebensohn et al., 2008; Lebensohn and Rollett, 2020), coupled with the modelling platform Elle (Bons et al., 2008; Piazolo et al., 2019), to illustrate the fold geometries that form when ice Ih with a mechanical anisotropy is shortened. The code has been used to simulate microstructural developments in deforming ice (Llorens et al., 2016, 2017; Steinbach et al., 2016) and the formation of folds and other structures in intrinsically anisotropic rocks (Ran et al., 2019; de Riese et al., 2019; Hu et al., 2024). The VPFFT code simulates deformation of a crystalline material by glide along crystallo-

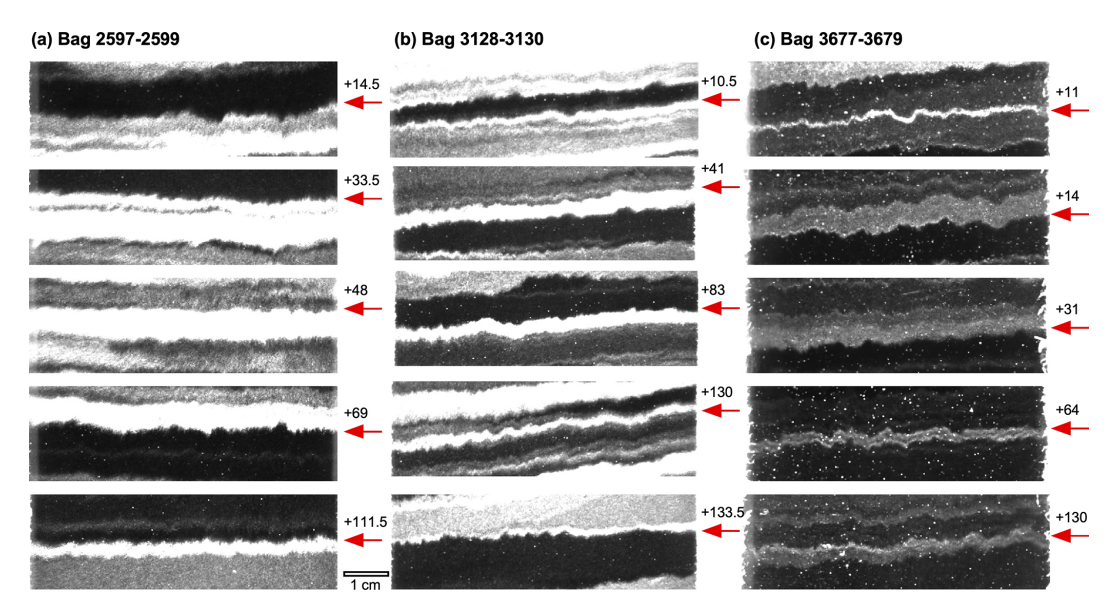


**Figure 4.** Images of all 15 cloudy-band interfaces (red arrows) that were analysed in this study. Red arrows indicate the analysed cloudy-band interface, with the distance from the top of the line-scan image given in cm.

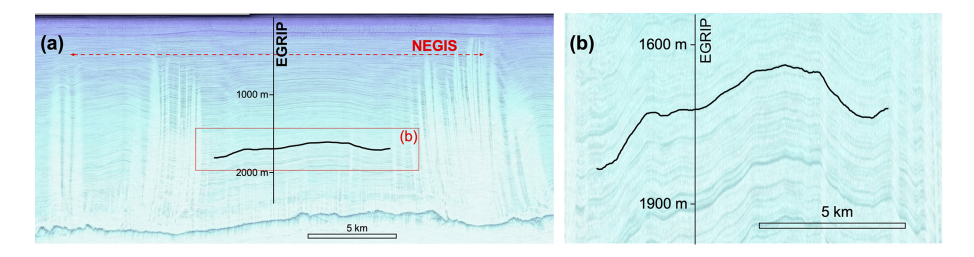


**Figure 5.** Traced internal reflection horizon (IRH) in a radargram going through NEGIS perpendicular to the ice flow (ice flow into the page) at the location where the EGRIP ice core is drilled. The radargram shown in panel (a) with a 4.3× vertical exaggeration is composed of profiles 20180508\_06\_004 and 20180514\_03\_001 (Franke et al., 2025, 2022b). (b) The same profile showing only the centre of NEGIS at an 18.2× vertical exaggeration at which the layer intersecting EGRIP at 1720 m depth was manually traced.

graphic planes. We use the crystallography of hexagonal ice Ih, which is mechanically highly anisotropic due to a much easier glide along its basal planes, compared to the glide along the prismatic and pyramidal slip systems (Duval et al., 1983). This crystal symmetry approximates a transversely isotropic material (Griera et al., 2013). We use a stress variable of 4 (Goldsby and Kohlstedt, 2001; Bons et al., 2018) for the power-law relation between strain rate and stress and assign a 16-times-higher slip resistance to the non-basal slip systems. At a given strain rate, the stress difference between the basal and non-basal slip systems is thus a factor of 16. This factor may actually underestimate the anisotropy, as it is about 60 according to Duval et al. (1983). In line with Llorens et al. (2017), we use a lower factor of 16 for numerical stability. Details of this modelling approach can be found in Griera et al. (2013) and Llorens et al. (2017).

The 2D models consist of an initially square  $256 \times 256$  grid of so-called "unodes" (Bons et al., 2008) that store the local lattice orientation. The unodes effectively represent crys-

tallites with a constant internal crystal orientation, defined by three Euler angles. Using a Potts model, we create 1995 grains that are, on average,  $6 \times 6$  unodes in size. All unodes inside one grain initially have the same lattice orientation. The lattice orientation of each grain is randomly drawn from a point maximum (with a standard deviation of  $10^{\circ}$ ) parallel to the vertical extension direction. Easy-glide basal planes are thus preferentially aligned parallel to the horizontal shortening direction, with a standard deviation of  $10^{\circ}$ . Using velocity boundary conditions, the square model is deformed by horizontal shortening of 2 % per calculation step up to 40 % shortening, accommodated by vertical stretching.

#### 3.2.2 Fold analysis

Between the two end-member fold shapes of box and chevron folds, folds resemble a wave or the addition of multiple waves. Not surprising, Fourier analyses have been applied to folds for about 50 years (Hudleston, 1973; Ramsay and Huber, 1987; Schmalholz and Mancktelow, 2016). This

can be used to determine whether the fold train has a single dominant wavelength or is composed of folds of different wavelengths (Fig. 2). We therefore applied a fast Fourier transform (FFT) to fold contours of both natural and numerical folds. For this, we created bitmap images of the folds to analyse, with the fold trace drawn as a black line of a few pixels' width, roughly parallel to the x axis. A script selected the y coordinates of the middle of the line for each x coordinate along the trace. The equidistant x, y data were then detrended by subtracting a linear least-squares best fit through the x, y data. The detrended series of y data was then subjected to a discrete Fourier transform using the routine four1() of Press et al. (1992). The power spectrum was obtained by taking the square root of the sum of the squares of the real and imaginary parts of the transform for each wavelength.

An example of the result is given in Fig. 7a, in which the input was a graph of a cosine function with a wavelength of 140 pixels and an amplitude (as defined in Fig. 2a) of 50 pixels. The FFT routine gives the power for wavelengths  $\lambda = W/n$ , where W is the width of the y series and n is a whole number greater or equal to 1. The nearest wavelength to  $\lambda = 140$  pixels of the cosine signal is 142.9 pixels (n = 7, for a series of 1000 pixels in length). The amplitude obtained for this wavelength is 35 instead of 50 pixels (Fig. 4a). This is for two reasons: (i) the wavelength is not exactly that of the real wavelength of the cosine signal, and (ii) rounding errors in the digitization of the signal affect the whole signal. Whereas wavelengths other than 140 should be 0, we see that they are not in the FFT analysis but are still distinctly lower than the dominant wavelength.

We used three  $2044 \times 31550$  8-bit images of cloudy bands in the line scans of the EGRIP drill core with a resolution of  $18.6 \,\mathrm{pixel\,mm^{-1}}$ . Images "bag 2597" (Fig. 4a) and "bag 3128" (Fig. 4b) had a suitable contrast, but a ca. 2× contrast stretch was applied to "bag 3677" (Fig. 4c) to achieve a sufficient contrast between dark and bright cloudy bands. In each bag, five boundaries between dark and bright cloudy bands were selected that were both sharp and where the adjacent cloudy bands showed no significant lateral variation in thickness. A selection of the image was then subjected to a median filter with a 4-pixel radius to reduce small-scale noise and then thresholded to a binary image. The folded trace was subsequently selected by edge detection between the now black-and-white bands, resulting in the lines shown in Fig. 6a. Only the middle 65 mm of the ca. 70 mm wide drill-core image was used to avoid artefacts at the edges of the image. The selection was scaled to an image with a width of 1024 pixels, or 65 mm. All this was done with the freeware ImageJ (Schneider et al., 2012). A script selected the y coordinates of the line for each x coordinate along the trace. The equidistant x, y data were then detrended by subtracting a linear least-squares best fit through the x, y data. The detrended series of 1024 y data was then subjected to a discrete Fourier transform using the routine four1() of Press et al. (1992). The power spectrum was obtained by taking the square root of the sum of the squares of the real and imaginary parts of the transform for each wavelength.

For the power spectrum of the numerical folds of Llorens et al. (2013), we applied the above method to a black-andwhite image of one of the modelled folds (Fig. 6c) in that paper to convert to the upper boundary of the folded layer in a set of 1024 equidistant x, y coordinates. For the largescale folds in NEGIS, we used a radargram that spans NEGIS (Franke et al., 2022b) and is located closely (a few metres) to the EGRIP ice core (Fig. 5) and chose a conspicuous layer at the depth of "bag 3128" (1719.85 m). Note that this layer in the radargram cannot be correlated directly with any specific cloudy band in the drill core. The layer was traced for 10 km only within NEGIS to avoid effects of the higher strain in the shear margins (Jansen et al., 2024). The image on which the layer was traced had a 18.2× vertical exaggeration. For the folded schist, we used a 3008 × 2000 pixel field photograph (Fig. 3b). In each case, the selected folded surface was hand-traced in a drawing program (Canvas12) to create a line that was further processed the same way as the cloudy-band interfaces.

In case of folds in an anisotropic material, simulated with Elle-VPFFT, a straight horizontal line, consisting of 102 400 nodes, at a chosen level in the model was subjected to deformation according to the velocity field that Elle-VPFFT records for each deformation step, up to the strain for which the power spectrum was to be calculated (Fig. 6b). The resulting line was then divided into  $256 \ x$ , y coordinates that are equidistant in the x direction by interpolating between the original nodes, after which the procedure was the same as for digitized folds in the cloudy bands. Linear least-squares best fits were applied to the  $\log(A)$  versus  $\log(\lambda)$  data of the power spectra to obtain the scaling variable s (Eq. 2) using the freeware Past4, except for the single-layer buckle fold, where Eq. (2) does not apply.

#### 4 Results

Below, we first present the power spectra for the single-layer buckle fold (Fig. 6c), the biotite schist (Fig. 3b), and the Elle-VPFFT simulation (Fig. 6b), as the folding mechanism is known in these cases. These results are then compared with those for the folds in ice.

#### 4.1 Single-layer buckle folds simulation

Llorens et al. (2013) used finite-element modelling for folding of a competent single layer in a homogeneous softer matrix. They used an isotropic power-law rheology relating strain rate  $(\dot{\varepsilon})$  to differential stress  $(\sigma)$ :

$$\dot{\varepsilon} = B \cdot \sigma^n. \tag{3}$$

Here, B is the pre-exponential factor, and n is the stress variable, which was set at n = 3. We show (Fig. 7b) the

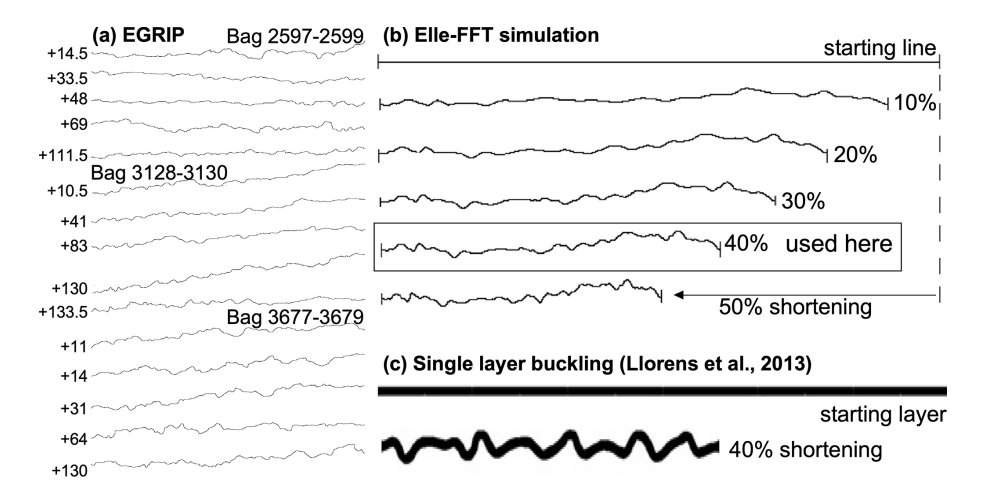


**Figure 6.** Fold traces. (a) Traces of folded cloudy-band interfaces in the EGRIP drill-core bags 2597, 3128, and 3677. Numbers on the left indicate the distance in cm from the top of the 165 cm long line-scan image. (b) Traces of an originally horizontal line at different amounts of horizontal shortening in a simulation with Elle-FFT with pure ice Ih (n = 4) and initially a horizontal alignment of the basal planes. (c) Example from Fig. 7c in Llorens et al. (2013) of single-layer buckling in a power-law material (n = 3).

power spectrum for 40 % layer-parallel shortening of a layer of original length 100 and unit thickness. The layer was made 25 times stronger than the matrix by setting  $B_{\rm matrix} = 25 \times B_{\rm layer}$ . The resulting fold (Fig. 6c) shows eight to nine distinct antiforms in the fold train but no clear folds with other wavelengths. The power spectrum (Fig. 7b) shows a distinct peak at ca. 7.5 times the original layer thickness for a fold-train length of 60 after 40 % shortening. The initial wavelength was thus about 11–12 times the layer thickness. The simulation confirms that a dominant wavelength develops in the case of Biot-type folding.

#### 4.2 Folded biotite schist

The folded foliation in the biotite schist from Puig de Culip (Fig. 3b) shows a power spectrum with a steady increase in the amplitude with the wavelength (Fig. 7c). A power-law best fit results in a variable of approximately s=1, implying that the amplitude is linearly proportional with the wavelength (Eq. 2) and the folds are approximately self-similar. The image of the biotite schist (Fig. 3b) shows that a composite layering is absent but that the platy biotite crystals form a strong foliation that is folded. The self-similarity of these folds confirms that Eq. (2) applies for folds that are due to an intrinsic mechanical anisotropy.

## 4.3 Elle-FFT simulation

We analysed 10 equally spaced originally horizontal lines in the model of folding in ice with aligned basal planes (Fig. 8). We chose a finite strain of 40 % shortening, as the lines folded to achieve relative arc lengths of  $1.14 \pm 0.2$ , comparable to those obtained from the cloudy bands (see below). Initially, horizontal lines were folded with various wavelengths. Medium to large folds can be traced along their axial planes

over many lines, suggesting that the folds are more harmonic than those in the cloudy bands if the model is assumed to have a width comparable to that of the EGRIP drill core.

The power spectrum shows a steady increase in power with wavelength from  $\lambda \approx 5$  initial element widths (Fig. 7d), which is on the order of the mean grain width after 40 % horizontal shortening and  $A_{(\lambda)}$  increases approximately linearly with increasing  $\lambda$ , i.e.  $s \approx 1$ . This means that the folds are self-similar: their shape is independent of their wavelength.

#### 4.4 Cloudy bands

Cloudy bands have a variety of thicknesses, ranging from about a mm to a few cm (Figs. 1 and 4). However, it is difficult to define the thickness of one band, as what appears like one dark or bright band may itself be composed of several thinner bands of different brightness (Stoll et al., 2023). All interfaces are folded on the mm to cm scale (Figs. 1 and 4). Folding is most conspicuous in the interfaces of very bright and very dark bands. The folds are upright with mostly vertical axial planes (Fig. 1b), although some zones with tilted axial planes have been observed (Westhoff et al., 2021). Folds are disharmonic, meaning that individual axial planes can rarely be traced from one interface to another, i.e. for more than about 5 mm (Fig. 1). This means that the folds in individual interfaces appear independent of those in the next. Relative arc length ratios of the 15 folded interfaces are, on average, 1.15 ( $\pm 0.03$  standard deviation).

The individual and average power or amplitude spectra of the 15 folded interfaces at the three selected depths show no significant differences. We therefore averaged the powers for each wavelength, as shown (Fig. 9a). We see that the amplitudes show a linear ( $s \approx 1$ ) increase up to about  $\lambda = 20$  mm. The amplitudes of the largest two wavelengths are below the

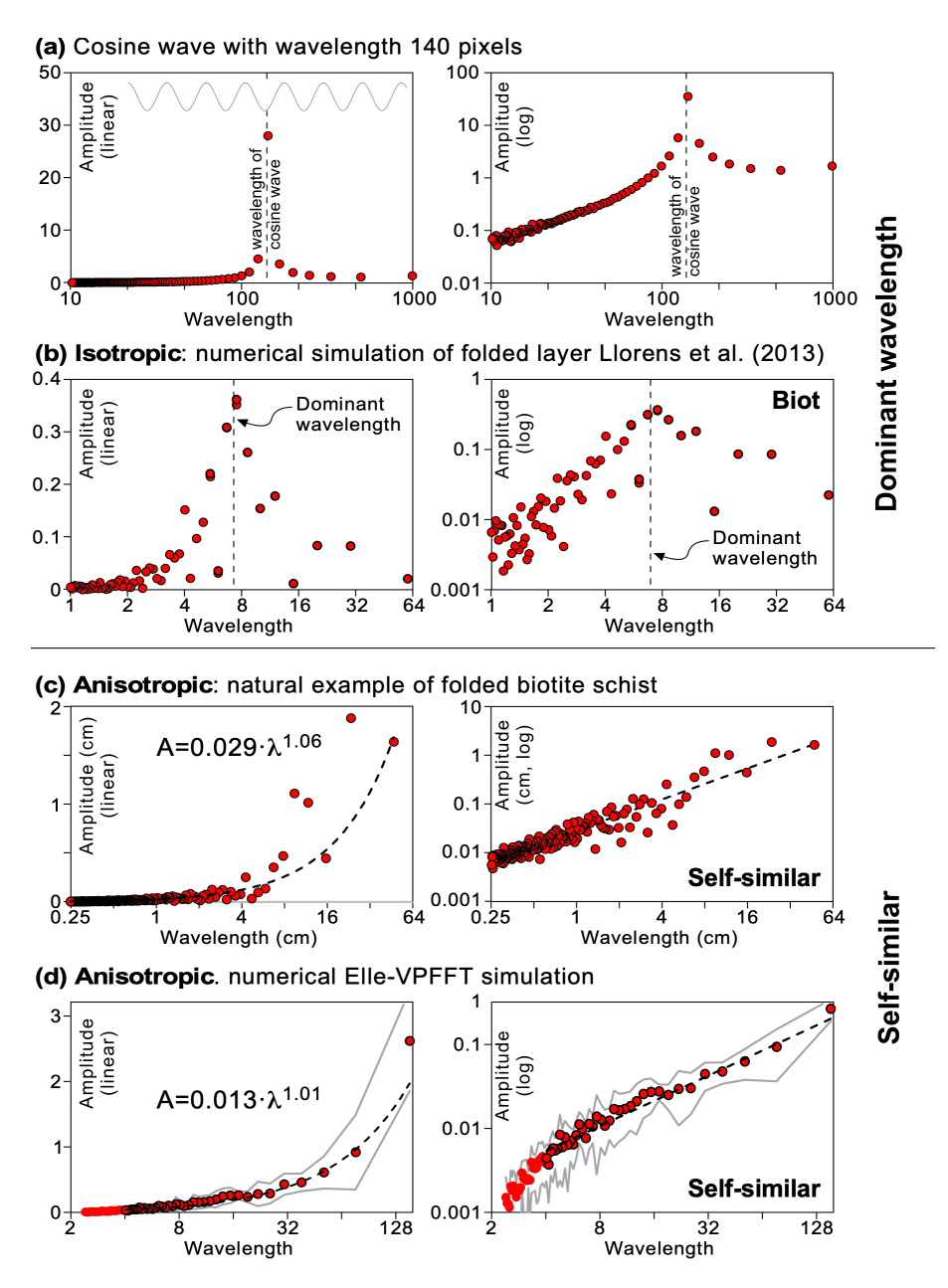


**Figure 7.** Power spectra of analysed folds. The vertical axis showing the amplitude is linear in the left column and logarithmic in the right column. (a) Power spectrum of a regular cosine wave. (b) Numerical simulation of a single layer in a homogeneous and isotropic softer matrix (Llorens et al., 2013). The power spectrum shows a distinct peak at a wavelength of ca. 7.5 length units with a total length of the fold train of 60 units. The layer had an initial length of 100 units. (c) Folded foliation in the biotite schist from Puig de Culip shows an approximately self-similar power-law power spectrum. (d) Numerical simulation with Elle-VPFFT of the folding of intrinsically anisotropic, pure ice that has an initial strong alignment of basal planes parallel to the shortening direction. Dots are the average of datasets in the model, while grey lines show the one standard deviation variation. The power spectrum follows an approximately self-similar power law from a wavelength of about five element widths of the initial  $256 \times 256$  model.

trend, but it cannot be ascertained whether this is significant or merely due to the large variation in amplitudes. No dominant wavelength well below 65 mm was observed.

#### 4.5 Large-scale folds inside NEGIS

The radargram shows a traceable reflector that crosses the EGRIP drill core at about 1720 m depth, which is the depth of bags 3128–3130 from which cloudy bands were analysed. This does not mean that the reflector is directly comparable

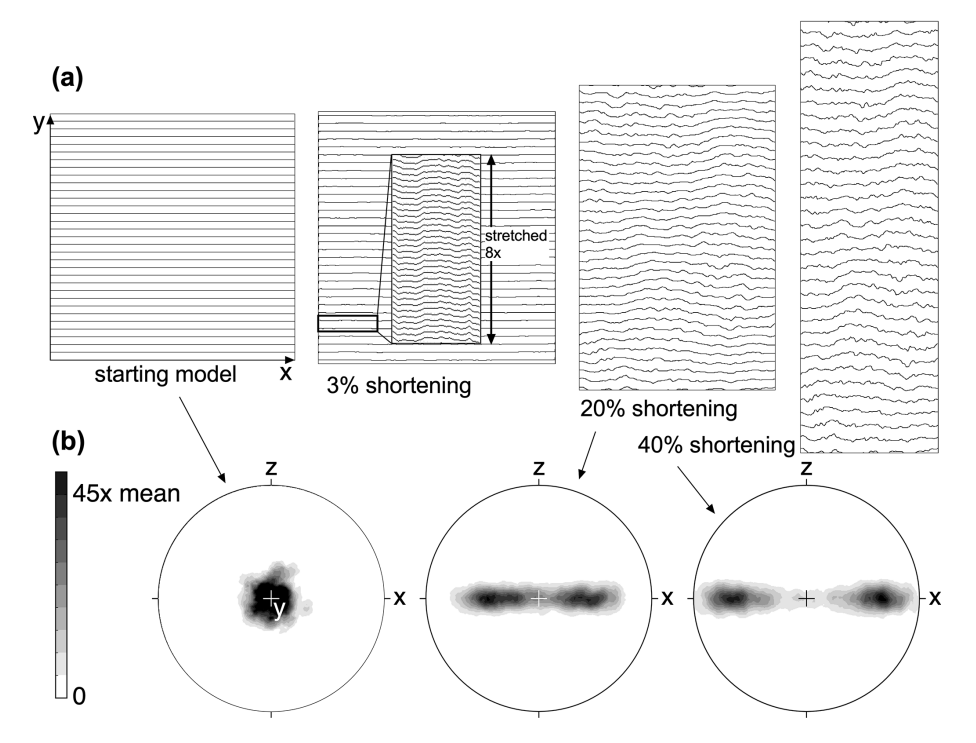


**Figure 8.** Result of the Elle-VPFFT simulation showing the model at 0, 3, 20, and 40 % horizontal (x axis) shortening that is compensated by vertical (y axis) stretching in the plane strain. (**a**) Passive markers originally aligned to the horizontally aligned basal planes. At 3 % shortening, folds can barely be discerned. At 8× vertical stretching, the initial folds become visible. These have relatively straight limbs and sharp hinges compared to folds at higher strains. (**b**) Stereographs of the c-axis orientations looking down along the vertical y axis. Plots were created with Stereonet by F. W. Vollmer, using orientations of 2500 randomly selected elements out of a total of 65 536 elements. Note that in NEGIS, horizontal shortening is not compensated in the vertical direction but rather in the horizontal flow direction. This would reduce fold amplification but not the fold pattern.

to any single cloudy band that is observed in the core at this depth. The 1720 m depth layer in NEGIS shows a power-law amplitude-wavelength trend with  $s \approx 1.5$  upwards from  $\lambda = 100$  m (Fig. 9b). This indicates that there is no characteristic wavelength and also that small folds are flatter in shape than large folds. A second layer at only 475 m below the surface shows the same trend as the 1720 m layer but shifted downwards (Fig. 9b). These folds thus have the same overall shape but smaller amplitudes. However, the fold trace may be too smooth on the small scale to correct for small vertical shifts and steps in reflector depths that are artefacts related to surface elevation variations. Underestimating amplitudes at low wavelengths would artificially increase the variable s.

## 5 Discussion

Folds in the cloudy bands do not show a dominant wavelength in the wavelength range shorter than the width of the drill-core section (Fig. 9a). The power spectra of the 15 sampled fold traces all overlap and show no significant variation between them, although the cloudy bands that are immediately adjacent vary in thickness from 1 to >10 mm. Both observations suggest that the folding has no characteristic length scale. In the case of Biot-type buckle folding,

this characteristic length scale would be the thickness of the layers, here the cloudy bands. For Biot-type buckle folding, one would expect shorter wavelength folds in the ca. 1 mm thick cloudy band 3677 + 11 than in the 10 times thicker one at 3677 + 14. Multi-wavelength folds can develop in multilayers (e.g. Fig. 11 in Frehner and Schmalholz, 2006). These form by the addition of different characteristic wavelengths of layers with different thickness and/or rheology. However, harmonic folds are then expected with axial planes extending across several layers that contribute to the multi-wavelength folds. For the analysed cloudy bands, this is not the case, as the axial planes rarely extend for more than 5–10 mm. These observations suggest that the folds in the cloudy bands are not the result of Biot-type buckling due to rheological differences between individual cloudy bands, where a high viscosity contrast between layers ( $\geq 25$ ) is required for folding (Llorens et al., 2013).

The cloudy-band folds resemble folds in the biotite schist (Figs. 3b, 7c) and the numerical ELLE-FFT folds in ice with a strong CPO (Figs. 7d, 8) much more than Biot-type buckle folds (Figs. 3a, 6c, 7b). This holds for both a visual assessment and for the power spectra. Shortening parallel to an intrinsic initial (before the onset of folding) mechanical

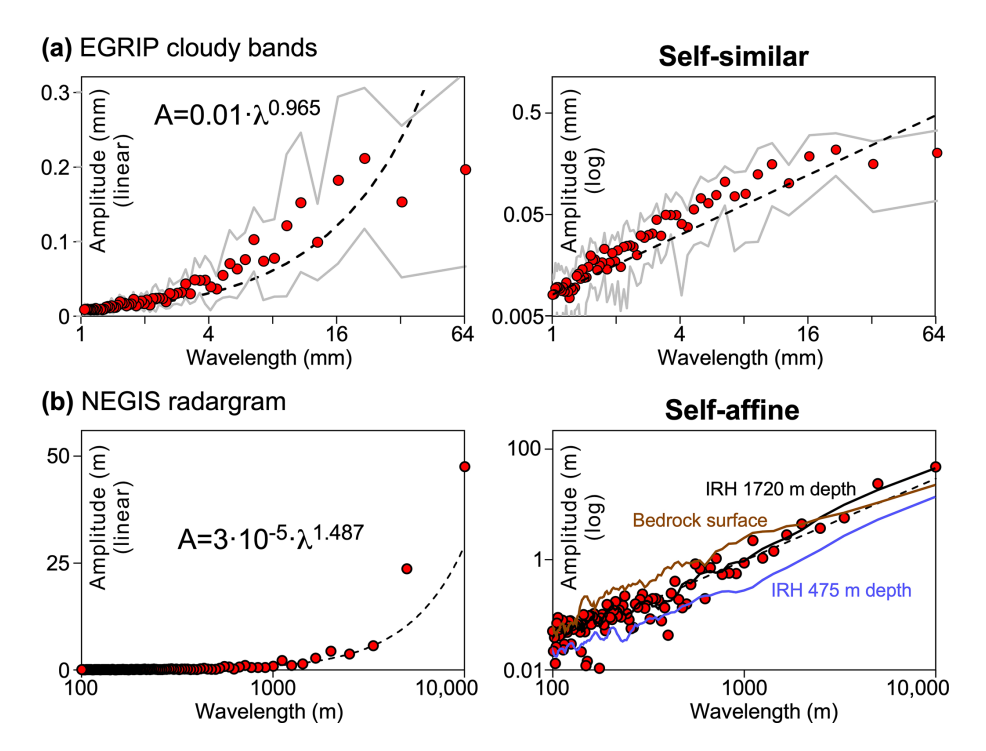


Figure 9. Power spectra for folds in ice. (a) Average power spectrum of all 15 cloudy-band interfaces (red dots), shown together with plus/minus one standard deviation (grey lines) of the variation in powers. The data roughly follow a self-similar power law up to  $l \approx 20$  mm. (b) Power spectrum for the internal reflection horizon (IRH) in the radargram that intersects the EGRIP drill core at ca. 1720 m depth (Fig. 5) traced over a distance of 10 km perpendicular to NEGIS' flow direction. A power-law best fit for  $\lambda \ge 100$  m results in a scaling variable of  $s \approx 1.5$ . The vertical amplitude axis is linear in the left column and logarithmic in the right column.

anisotropy due to a CPO is therefore the preferred mechanism to explain the observed folding in the cloudy bands, as was already suggested by Jansen et al. (2016). We observe a similar lack of a characteristic wavelength in the large-scale folds inside NEGIS (Fig. 9). This supports the suggestion by Bons et al. (2016) and the numerical simulations by Zhang et al. (2024) that such large-scale folding is also due to shortening parallel to the CPO-induced anisotropy.

The cloudy bands and internal reflection horizons are thus passive material planes whose folds reveal the heterogeneity of deformation due to CPO-induced anisotropy. This CPO was probably a vertical single maximum of the c-axis orientations. However, folding, of course, changes this CPO, resulting in a girdle with (Fig. 8b) or without (Stoll et al., 2023) two maxima. The passive marker planes do not reflect the current CPO but the cumulative heterogeneous strain resulting from the evolving CPO.

A power-law best fit through the combined cloudy-band and radargram folds results in a scaling variable of  $s \approx 0.83$  (Fig. 10, Table 1). This would mean that the folds gradually get flatter with increasing scale, implying that the scales are related and that the folds are self-affine (Fig. 2d). Reasons for this could be the effect of the ice-sheet surface, where gravity and ice precipitation counteract the development of surface topography due to folding (Waddington et al., 2001; Zhang et al., 2024). An additional effect could be

the bedrock topography or bedrock processes (Bell et al., 2014; Wolovick et al., 2014; Leysinger-Vielli et al., 2018) that impose additional folding or fold-amplitude modifications of the anisotropy-induced folds (Fig. 10). Unfortunately, we do not have sufficiently detailed observations in the length-scale range from 10 cm to about 100 m. It is therefore possible that the power spectra between the small and large scale show a break. If one would extend the self-similar  $(s \approx 1)$  trend of the cloudy-band folds up to 10 km, expected fold amplitudes are close to those of the largest wavelengths in the radargram folds (Fig. 10). The deviation in scaling variable at the large scale would then be a result of smoothing of folds with  $\lambda < 100$  m in the radargram. Unfortunately, the radargrams do not provide sufficient resolution for the detailed fold analyses that are applied here. Looking forward, future studies could benefit from higher-resolved radar data products to better characterize smaller-scale folds in internal reflection horizons. The dataset used in this study was limited to a vertical resolution of  $\sim 4.3$  m due to the system bandwidth of 30 MHz. Future deployments using broader bandwidth systems and optimized acquisition and processing strategies to increase range and along-track resolution could extend the detectable wavelength range of folded horizons. This would help bridge the resolution gap between drill-core observations and radar-imaged folds, thereby refining our understanding of anisotropy-induced deformation across scales.

Table 1. Results of power-law fits to the different fold sets.

| Fold set           | λ range                                 | Best fit s | s range       | $r^2$ |
|--------------------|---|------------|---------------|-------|
| Biotite schist     | 0.25–47 cm                              | 1.057      | 0.976-1.152   | 0.90  |
| Elle+VPFFT         | 5–153 relative to original width of 256 | 1.010      | 0.935 - 1.087 | 0.68  |
| Cloudy bands       | 1–65 mm                                 | 0.965      | 0.884 - 1.047 | 0.58  |
| NEGIS              | 100 m–10 km                             | 1.487      | 1.39-1.62     | 0.86  |
| NEGIS+cloudy bands | 3 mm–10 km                              | 0.827      | 0.80 – 0.86   | 0.99  |

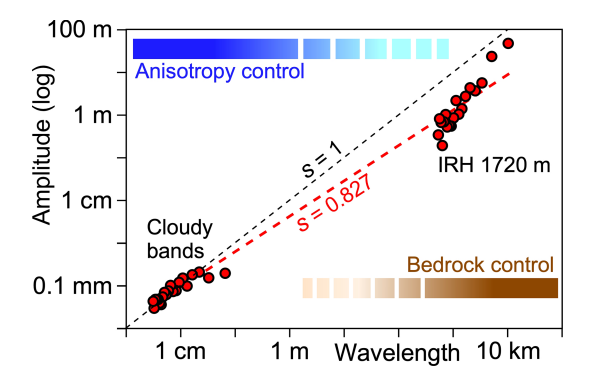


**Figure 10.** Combined power spectra of cloudy-band interfaces and the internal reflection horizon (IRH), showing the 40 largest wavelengths of each spectrum. A power-law best fit through these data gives a variable s = 0.827, suggesting that folding is self-affine (Fig. 2d), with large folds being relatively flat compared to small folds.

Having argued that folding in cloudy bands in ice sheets is the result of shortening of an intrinsic anisotropy, we now briefly address the degree of anisotropy. Materials with a very strong transverse isotropy tend to form kink or chevron-type folds (Cobbold et al., 1971; Ramsay, 1974; Nabavi and Fossen, 2021). Such chevron folds, or "fabric stripes", have been described in ice with a strong CPO (Alley et al., 1997; Jansen et al., 2016). With decreasing degree of anisotropy, folds become more rounded, and axial planes are oriented perpendicular to the direction of maximum shortening (Cobbold et al., 1971), as is the case for the folds in cloudy bands shown here (Fig. 4). The ELLE-VPFFT simulation started with a strong single-maximum CPO (Fig. 8b). Initial (3 % shortening) folds are relatively chevron-like. Such a low strain is comparable with the model proposed by Jansen et al. (2016), where chevron-type fabric stripes develop in simple shear with a c-axis single maximum almost perpendicular to the shear plane. The situation is different in pure shear shortening, which leads to stronger shortening of the cloudy bands that are initially perpendicular to the preferred c-axis orientation. In this case, both the CPO and the CPO-induced mechanical anisotropy evolve (Fig. 8b) together with the folding of the cloudy bands, leading to more rounded folds at all scales.

In the absence of any other factors that control folding, the proportionality factor  $(\lambda_0)$  in Eq. (2) should depend only on the type of anisotropy, its intensity, and the amount of shortening. This implies that it should be possible to determine the actual anisotropy of ice with folds (e.g. the EGRIP drill core) if the initial CPO can be constrained and the amount of shortening parallel to the folded planes (e.g. the cloudy bands) is known. This could be a helpful independent estimate of the anisotropy of flowing ice and, hence, its effective hardening or softening due to the flow field, in addition to other studies (Gerber et al., 2023). This is, however, well beyond the scope of this study.

#### 6 Conclusions

We used power spectra of fold traces to determine the mechanism for folding in ice sheets. Biot-type buckle folds due to rheological contrasts between layers have a characteristic length scale, related to the layer thickness and the rheological contrast between the layers that are internally isotropic. A numerical simulation of ice with a strong alignment of basal planes parallel to the shortening direction resulted in the development of self-similar folds with a power-law power spectrum. This is to be expected, as anisotropy has no length scale. Self-similar folds were also observed in folded biotite schist and in cloudy bands in the EGRIP drill core. We therefore conclude that small-scale folds in cloudy bands are due to shortening parallel to a strong anisotropy as a result of the lattice preferred orientation with initially horizontally aligned basal planes. Combining the small cloudy-band folds and large NEGIS-scale folds resulted in a self-affine trend, where the largest folds are relatively flat. This may be caused by additional boundary conditions, such as vertical flattening and bedrock irregularities, that modify the anisotropyinduced folds on the large scale.

Code availability. The updated version of the Elle+FFT software package from Hao et al. (2023a) can be downloaded from https://doi.org/10.5281/zenodo.10259841 (Hao et al., 2023b). We recommend using the Elle+FFT software package by Singularity container under Linux (e.g. for Ubuntu 20.04). Additional information on the software can be found in the Appendix section of the PhD thesis of Florian Steinbach, which can be downloaded

from the library of Tübingen University (https://publikationen. uni-tuebingen.de/xmlui/handle/10900/76435, last access: 23 August 2025). The Elle+VPFFT input files (ASCII text files) to rerun the simulations used in this paper can be downloaded as Supplement.

Data availability. Visual stratigraphy data from the EastGRIP ice core are available at https://doi.org/10.1594/PANGAEA.925014 (Weikusat et al., 2020). The radio-echo sounding data shown in Fig. 5 (profile IDs: 20180508\_06\_004 and 20180514\_03\_001) from AWI's EGRIP-NOR-2018 survey are available under https://doi.org/10.1594/PANGAEA.928569 (Franke et al., 2025, 2022b). Input files for the Elle+VPFFT numerical simulation shown here (folder supplement\_Elle\_VPFFT\_files) are provided as Supplement to this article. The data contain x, y coordinates of all analysed fold trains as tab-delimited ASCII text files.

*Supplement.* The supplement related to this article is available online at https://doi.org/10.5194/tc-19-5095-2025-supplement.

Author contributions. PDB conceived the study, performed most analyses, and wrote the paper. JW, NS, and IW acquired and processed the visual stratigraphy data. MGL, YH, and YZ carried out numerical simulations and contributed to modelling efforts. SF processed and contributed radar data. All authors jointly contributed to the discussion of the results and reviewed the paper.

Competing interests. The contact author has declared that none of the authors has any competing interests.

Disclaimer. Publisher's note: Copernicus Publications remains neutral with regard to jurisdictional claims made in the text, published maps, institutional affiliations, or any other geographical representation in this paper. While Copernicus Publications makes every effort to include appropriate place names, the final responsibility lies with the authors. Views expressed in the text are those of the authors and do not necessarily reflect the views of the publisher.

Acknowledgements. We acknowledge the use of software from Open Polar Radar generated with support from the University of Kansas, NASA grants 80NSSC20K1242 and 80NSSC21K0753, and NSF grants OPP-2027615, OPP-2019719, OPP-1739003, IIS-1838230, RISE-2126503, RISE-2127606, and RISE-2126468. EastGRIP is directed and organized by the Centre for Ice and Climate at the Niels Bohr Institute, University of Copenhagen. It is supported by funding agencies and institutions in Denmark (A. P. Møller Foundation, University of Copenhagen), the USA (US National Science Foundation, Office of Polar Programs), Germany (Alfred Wegener Institute, Helmholtz Centre 475 for Polar and Marine Research), Japan (National Institute of Polar Research and Arctic Challenge for Sustainability), Norway (University of Bergen and Trond Mohn Foundation), Switzerland (Swiss National Sci-

ence Foundation), France (French Polar Institute Paul-Emile Victor, Institute for Geosciences and Environmental research), Canada (University of Manitoba), and China (Chinese Academy of Sciences and Beijing Normal University). Julien Westhoff acknowledges funding from Villum Investigator project IceFlow (grant no. 16572). Yu Zhang was funded by the China Scholarship Council (Grant number 202006010063). Yuanbang Hu was funded by the China Scholarship Council (grant number 202008510177). Steven Franke was funded by the Walter Benjamin Programme of the Deutsche Forschungsgemeinschaft (DFG, German Research Foundation; project number 506043073). Nicolas Stoll acknowledges funding from the Programma di Ricerche in Artico (PRA) and the German Academic Exchange Service (DAAD, Postdoc Fellowship RESTORATION). Nicolas Stoll further gratefully acknowledges funding from the European Union's Horizon 2020 research and innovation programme under the Marie Skłodowska-Curie grant agreement no. 101146092.

Financial support. This research has been supported by the Villum Fonden (grant no. 16572), the China Scholarship Council (grant nos. 202008510177 and 202006010063), the Programma di Ricerche in Artico (PRA), the German Academic Exchange Service (DAAD), the Marie Skłodowska-Curie programme (grant no. 101146092), and the Deutsche Forschungsgemeinschaft (grant no. 506043073).

This open-access publication was funded by the Open Access Publication Fund of the University of Tübingen.

*Review statement.* This paper was edited by Carlos Martin and reviewed by two anonymous referees.

#### References

Alley, R. B., Gow, A. J., Meese, D. A., Fitzpatrick, J. J., Waddington, E. D., and Bolzan, J. F.: Grain-scale processes, folding, and stratigraphic disturbance in the GISP2 ice core, J. Geophys. Res.,102, 26819–26830, https://doi.org/10.1029/96JC03836, 1997.

Bell, R. E., Tinto, K., Das, I., Wolovick, M., Chu, W., Creyts, T. T., Frearson, N., Abdi, A., and Paden, J. D.: Deformation, warming and softening of Greenland's ice by refreezing meltwater, Nature Geoscience, 7, 497–502, https://doi.org/10.1038/ngeo2179, 2014.

Biot, M. A.: Folding Instability of a Layered Viscoelastic Medium under Compression, Proceedings of the Royal Society A: Mathematical, Physical and Engineering Sciences, 242, 444–454, https://doi.org/10.1098/rspa.1957.0187, 1957.

Bohleber, P., Stoll, N., Rittner, M., Roman, M., Weikusat, I., and Barbante, C.: Geochemical characterization of insoluble particle clusters in ice cores using two-dimensional impurity imaging, Geochemistry, Geophysics, Geosystems, 24, e2022GC010595, https://doi.org/10.1029/2022GC010595, 2023.

- Bons, P. D., Druguet, E., Hamann, I., Carreras, J., and Passchier, C. W.: Apparent boudinage in dykes, J. Struct. Geol., 26, 625–636, https://doi.org/10.1016/j.jsg.2003.11.009, 2004.
- Bons, P. D., Koehn, D., and Jessell, M. W. (Eds.): Microdynamic Simulation, Lecture Notes in Earth Sciences 106, Springer, Berlin, 405 pp., ISBN 978-3-540-44793-1, 2008.
- Bons, P. D., Jansen, D., Mundel, F., Bauer, C. C., Binder, T., Eisen, O., Jessell, M. W., Llorens, M. G., Steinbach, F., Steinhage, D., and Weikusat, I.: Converging flow and anisotropy cause large-scale folding in Greenland's ice sheet, Nature communications, 7, 11427, https://doi.org/10.1038/ncomms11427, 2016.
- Bons, P. D., Kleiner, T., Llorens, M.-G., Prior, D. J., Sachau, T., Weikusat, I., and Jansen, D.: Greenland Ice Sheet: Higher nonlinearity of ice flow significantly reduces estimated basal motion, Geophys. Res. Lett., 45, 6542–6548, https://doi.org/10.1029/2018GL078356, 2018.
- Budd, W. F. and Jacka, T. H.: A review of ice rheology for ice sheet modeling, Cold Regions Science and Technology, 16, 107–144, https://doi.org/10.1016/0165-232X(89)90014-1, 1989.
- Carreras, J., Cosgrove, J. W., and Druguet, E.: Strain partitioning in banded and/or anisotropic rocks: Implications for inferring tectonic regimes, J. Struct. Geol., 50, 7–21, https://doi.org/10.1016/j.jsg.2012.12.003, 2013.
- Cobbold, P. R., Cosgrove, J. W., and Summers, J. M.: Development of internal structures in deformed anisotropic rocks, Tectonophysics 12, 23–53, https://doi.org/10.1016/0040-1951(71)90065-5, 1971.
- de Riese, T., Evans, L., Gomez-Rivas, E., Griera, A., Lebensohn, R. A., Llorens, M.-G., Ran, H., Sachau, T., Weikusat, I., and Bons, P. D.: Shear localisation in anisotropic, non-linear viscous materials that develop a CPO: A numerical study, J. Struct. Geol., 124, 81–90, https://doi.org/10.1016/j.jsg.2019.03.006, 2019.
- Druguet, E., Passchier, C. W., Carreras, J., Victor, P., and den Brok, S. W. J.: Analysis of a complex high-strain zone at Cap de Creus, Spain, Tectonophysics, 280, 31–45, https://doi.org/10.1016/S0040-1951(97)00137-6, 1997.
- Duval, P., Ashby, M., and Anderman, I.: Rate controlling processes in the creep of polycrystalline ice, J. Phys. Chem., 87, 4066– 4074, https://doi.org/10.1021/j100244a014, 1983.
- Faria, S. H., Freitag, J., and Kipfstuhl, S.: Polar ice structure and the integrity of ice-core paleoclimate records, Quaternary Sci. Rev., 29, 338–351, https://doi.org/10.1016/j.quascirev.2009.10.016, 2010.
- Faria, S. H., Weikusat, I., and Azuma, N.: The microstructure of polar ice, Part II: State of the art, Journal of Structural Geology, 61, 21–49, https://doi.org/10.1016/j.jsg.2013.11.003, 2014.
- Finch, M. A., Bons, P. D., Steinbacha, F., Griera, A., Llorens, M.-G., Gomez-Rivase, E., Ran, H., and de Riese, T.: The ephemeral development of C' shear bands: A numerical modelling approach, J. Struct. Geol., 139, https://doi.org/10.1016/j.jsg.2020.104091, 2020.
- Fitzpatrick, J. J., Voigt, D. E., Fegyveresi, J. M., Stevens, N. T., Spencer, M. K., Cole-Dai, J., Alley, R. B., Jardine, G. E., Cravens, E. D., Wilen, L. A., Fudge, T. J., and McConnell, J. R.: Physical Properties of the WAIS Divide ice core, J. Glaciol., 60, 1181–1198, https://doi.org/10.3189/2014JoG14J100, 2014.
- Franke, S., Bons, P. D., Westhoff, J., Weikusat, I., Binder T., Streng, K., Steinhage, D., Helm, V., Eisen, O., Paden, J. D., Eagles, G., and Jansen, D.: Holocene ice-stream shutdown and

- drainage basin reorganization in northeast Greenland, Nature Geoscience, 15, 995–1001, https://doi.org/10.1038/s41561-022-01082-2, 2022a.
- Franke, S., Jansen, D., Binder, T., Paden, J. D., Dörr, N., Gerber, T. A., Miller, H., Dahl-Jensen, D., Helm, V., Steinhage, D., Weikusat, I., Wilhelms, F., and Eisen, O.: Airborne ultrawideband radar sounding over the shear margins and along flow lines at the onset region of the Northeast Greenland Ice Stream, Earth Syst. Sci. Data, 14, 763–779, https://doi.org/10.5194/essd-14-763-2022, 2022b.
- Franke, S., Bons, P. D., Streng, K., Mundel, F., Binder, T., Weikusat, I., Bauer, C. C., Paden, J. D., Dörr, N., Helm, V., Steinhage, D., Eisen, O., and Jansen, D.: Three-dimensional topology dataset of folded radar stratigraphy in northern Greenland, Sci. Data, 10, 525, https://doi.org/10.1038/s41597-023-02339-0, 2023.
- Franke, S., Jansen, S., Binder, T., Paden, J. D., Dörr, N., Gerber, T. A., Miller, H., Dahl-Jensen, D., Helm, V., Steinhage, D., Weikusat, I., Wilhelms, F., and Eisen, O.: ARK 2018:
  AWI airborne ultra-wideband radar data over the shear margins at the onset region of the Northeast Greenland Ice Stream (NEGIS) (EGRIPNOR-2018 Project), PANGAEA [data set], https://doi.org/10.1594/PANGAEA.983191, 2025.
- Frehner, M. and Schmalholz, S. M.: Numerical simulations of parasitic folding in multilayers, Journal of Structural Geology, 28, 1647–1657, https://doi.org/10.1016/j.jsg.2006.05.008, 2006.
- Gerber, T. A., Lilien, D. A., Rathmann, N. M., Franke, S., Young, T. J., Valero-Delgado, F., Ershadi, M. R., Drews, R., Zeising, O., Humbert, A., Stoll, N., Weikusat, I., Grinsted, A., Hvidberg, C. S., Jansen, D., Miller, H., Helm, V., Steinhage, D., O'Neill, C., Paden, J., Gogineni, S. P., Dahl-Jensen, D., and Eisen, O.: Crystal orientation fabric anisotropy causes directional hardening of the Northeast Greenland Ice Stream, Nat. Commun., 14, 2653, https://doi.org/10.1038/s41467-023-38139-8, 2023.
- Glen, J. W.: The creep of polycrystalline ice, Proceedings of the Royal Society of London A: Mathematical, Physical and Engineering Sciences, 228, 519–538, https://doi.org/10.1098/rspa.1955.0066, 1955.
- Goldsby, D. L. and Kohlstedt, D. L.: Superplastic deformation of ice: Experimental observations, Journal of Geophysical Research, 106, 11017–11030, https://doi.org/10.1029/2000JB900336, 2001.
- Griera, A., Llorens, M.-G., Gomez-Rivas, E., Bons, P. D., Jessell, M. W., Evans, L. A., and Lebensohn, R.: Numerical modelling of porphyroclast and porphyroblast rotation in anisotropic rocks, Tectonophysics, 587, 4–29, https://doi.org/10.1016/j.tecto.2012.10.008, 2013.
- Hansen, L. N., Faccenda, M., and Warren, J. M.: A review of mechanisms generating seismic anisotropy in the upper mantle, Physics of the Earth and Planetary Interiors, 313, 106662, https://doi.org/10.1016/j.pepi.2021.106662, 2021.
- Hao, B., Llorens, M.-G., Griera, A., Bons, P. D., Lebensohn, R. A., Yu, Y., and Gomez-Rivas, E.: Full-Field Numerical Simulation of Halite Dynamic Recrystallization From Subgrain Rotation to Grain Boundary Migration, Journal of Geophysical Research: Solid Earth, 128, https://doi.org/10.1029/2023JB027590, 2023a.
- Hao, B., Llorens, M.-G., Griera Artigas, A., Bons, P. D., Lebensohn, R., Yu, Y., and Gomez-Rivas, E.: Full-field numerical simulation of halite dynamic recrystallization from

- subgrain rotation to grain boundary migration, in: Journal of Geophysical Research Solid Earth (1.0), Zenodo [code], https://doi.org/10.5281/zenodo.10259841, 2023b.
- Hu, Y, Bons, P.D., de Riese, T., Liu, S, Llorens, M.-G., González-Esvertit, E., Gómez-Rivas, E., Li, D., Fu, Y., and Cai, X.: Folding of a single layer in an anisotropic viscous matrix under layer-parallel shortening, J. Struct. Geol., 188, 105246, https://doi.org/10.1016/j.jsg.2024.105246, 2024.
- Hudleston, P. J.: An analysis of "single-layer" folds developed experimentally in viscous media, Tectonophysics, 16, 189–214, https://doi.org/10.1016/0040-1951(73)90012-7, 1973.
- Hudleston, P. J.: Structures and Fabrics in Glacial Ice: A Review, Journal of Structural Geology, 81, 1–27, https://doi.org/10.1016/j.jsg.2015.09.003, 2015.
- Jansen, D., Llorens, M.-G., Westhoff, J., Steinbach, F., Kipfstuhl, S., Bons, P. D., Griera, A., and Weikusat, I.: Small-scale disturbances in the stratigraphy of the NEEM ice core: observations and numerical model simulations, The Cryosphere, 10, 359–370, https://doi.org/10.5194/tc-10-359-2016, 2016.
- Jansen, D., Franke, S., Bauer, C. C., Binder, T., Dahl-Jensen, D., Eichler, J., Eisen, O., Hu, Y., Kerch, J., Llorens, M.-G., Miller, H., Neckel, N., Paden, J., Riese, T. de, Sachau, T., Stoll, N., Weikusat, I., Wilhelms, F., Zhang, Y., and Bons, P. D.: Shear margins in upper half of Northeast Greenland Ice Stream were established two millennia ago, Nat. Commun., 15, 1193, https://doi.org/10.1038/s41467-024-45021-8, 2024.
- Krabbendam, M.: Sliding of temperate basal ice on a rough, hard bed: creep mechanisms, pressure melting, and implications for ice streaming, The Cryosphere, 10, 1915–1932, https://doi.org/10.5194/tc-10-1915-2016, 2016.
- Lebensohn, R. A.: N-site modeling of a 3D viscoplastic polycrystal using Fast Fourier Transform, Acta Materialia, 49, 2723–2737, https://doi.org/10.1016/S1359-6454(01)00172-0, 2001.
- Lebensohn, R. A. and Rollett, A. D.: Spectral methods for full-field micromechanical modelling of polycrystalline materials, Computational Materials Science, 173, 109336, https://doi.org/10.1016/j.commatsci.2019.109336, 2020.
- Lebensohn, R. A., Brenner, R., Castelnau, O., and Rollett, A. D.: Orientation image-based micromechanical modelling of subgrain texture evolution in polycrystalline copper, Acta Materialia, 56, 3914–3926, https://doi.org/10.1016/j.actamat.2008.04.016, 2008.
- Leysinger-Vieli, G. J.-M. C., Martín, C., Hindmarsh, R. C. A., and Lüthi, M. P.: Basal freeze-on generates complex ice-sheet stratigraphy, Nat. Commun., 9, 4669, https://doi.org/10.1038/s41467-018-07083-3, 2018.
- Llorens, M. G.: Stress and strain evolution during single-layer folding under pure and simple shear, Journal of Structural Geology, 126, 245–257, https://doi.org/10.1016/j.jsg.2019.06.009, 2019.
- Llorens, M. G., Bons, P. D., Griera, A., Gomez-Rivas, E., and Evans, L. A.: Single layer folding in simple shear, J. Struct. Geol., 50, 209–220, https://doi.org/10.1016/j.jsg.2012.04.002, 2013.
- Llorens, M.-G., Griera, A., Bons, P. D., Roessiger, J., Lebensohn, R. A., Evans, L. A., and Weikusat, I.: Dynamic recrystallisation of ice aggregates during co-axial viscoplastic deformation: A numerical approach, J. Glaciol., 62, 359–377, https://doi.org/10.1017/jog.2016.28, 2016.

- Llorens, M.-G., Griera, A., Steinbach, F., Bons, P. D., Gomez-Rivas, E., Jansen, D., Roessiger, J., Levensohn, R. A., and Weikusat, I.: Dynamic recrystallisation during deformation of polycrystalline ice: insights from numerical simulations, Philosophical Transactions of the Royal Society A, Special Issue on Microdynamics of Ice, 375, 20150346, https://doi.org/10.1098/rsta.2015.0346, 2017.
- Nabavi, S. T. and Fossen, H.: Fold geometry and folding a review, Earth-Sci. Rev., 222, 103812, https://doi.org/10.1016/j.earscirev.2021.103812, 2021.
- NEEM community members: Eemian interglacial reconstructed from a Greenland folded ice core, Nature, 493, 489–494, https://doi.org/10.1038/nature11789, 2013.
- Panton, C. and Karlsson, N. B.: Automated mapping of near bed radio-echo layer disruptions in the Greenland Ice Sheet, Earth Planet. Sci. Lett., 432, 323–331, https://doi.org/10.1016/j.epsl.2015.10.024, 2015.
- Piazolo, S, Bons, P. D., Griera, A., Llorens, M.-G., Gomez-Rivas, E., Koehn, D., Wheeler, J., Gardner, R., Godinho, J. R. A., Evans, L., Lebensohn, R. A., and Jessell, M. W.: A review of numerical modelling of the dynamics of microstructural development in rocks and ice: Past, present and future, J. Struct. Geol., 125, 111–123, https://doi.org/10.1016/j.jsg.2018.05.025, 2019.
- Press, W. H., Teukolsky, S. A., Vetterling, W. T., and Flannery, B. P.: Numerical recipes in C, 2nd edn., Cambridge University Press, Cambridge, 994 pp., ISBN: 9780521437202, 1992.
- Ramsay, J. G.: Development of chevron folds, GSA Bulletin, 85, 1741–1754, https://doi.org/10.1130/0016-7606(1974)85<1741:DOCF>2.0.CO;2, 1974.
- Ramsay, J. G. and Huber, M. I.: The Techniques of Modern Structural Geology: Folds and Fractures, Vol. 2, Academic Press, London, https://doi.org/10.1017/S0016756800010384, 1987.
- Ran, H., de Riese, T., Llorens, M.-G., Finch, M. A., Evans, L. A., Gomez-Rivas, E., Griera, A., Jessell, M. W., Lebensohn, R. A., Piazolo, S., and Bons, P. D.: Time for anisotropy: The significance of mechanical anisotropy for the development of deformation structures, J. Struct. Geol., 125, 41–47, https://doi.org/10.1016/j.jsg.2018.04.019, 2019.
- Schmalholz, S. M. and Mancktelow, N. S.: Folding and necking across the scales: a review of theoretical and experimental results and their applications, Solid Earth, 7, 1417–1465, https://doi.org/10.5194/se-7-1417-2016, 2016.
- Schneider, C., Rasband, W., and Eliceiri, K.: NIH Image to ImageJ: 25 years of image analysis, Nat. Methods, 9, 671–675, https://doi.org/10.1038/nmeth.2089, 2012.
- Steinbach, F., Bons, P. D., Griera, A., Jansen, D., Llorens, M.-G., Roessiger, J., and Weikusat, I.: Strain localization and dynamic recrystallization in the ice–air aggregate: a numerical study, The Cryosphere, 10, 3071–3089, https://doi.org/10.5194/tc-10-3071-2016, 2016.
- Stoll, N., Westhoff, J., Bohleber, P., Svensson, A., Dahl-Jensen, D., Barbante, C., and Weikusat, I.: Chemical and visual characterisation of EGRIP glacial ice and cloudy bands within, The Cryosphere, 17, 2021–2043, https://doi.org/10.5194/tc-17-2021-2023, 2023.
- Stoll, N., Weikusat, I., Jansen, D., Bons, P., Darányi, K., Westhoff, J., Llorens, M.-G., Wallis, D., Eichler, J., Saruya, T., Homma, T., Rasmussen, S. O., Sinnl, G., Svensson, A., Drury, M., Wilhelms, F., Kipfstuhl, S., Dahl-Jensen, D., and Kerch, J.: Linking

- crystallographic orientation and ice stream dynamics: evidence from the EastGRIP ice core, The Cryosphere, 19, 3805–3830, https://doi.org/10.5194/tc-19-3805-2025, 2025.
- Svensson, A., Wedel Nielsen, S., Kipfstuhl, S., Johnsen, J., Steffensen, J. P., Bigler, M., Ruth, U., and Röthlisberger, R.: Visual Stratigraphy of the North Greenland Ice Core Project (North-GRIP) ice core during the last glacial period, J. Geophys. Res., 110, D02108, https://doi.org/10.1029/2004JD005134, 2005.
- Thorsteinsson, T.: Textures and fabrics in the GRIP ice core, in relation to climate history and ice deformation (Thesis), Berichte zur Polarforschung, AWI Bremerhaven, Bremerhaven, 120–133, https://doi.org/10.2312/BzP\_0205\_1996, 1996.
- Twiss, R. J. and Moores, E. M.: Structural Geology, 2nd ed.: xvi + 736 pp., New York: W. H. Freeman, ISBN 9780716749516, Geological Magazine, 145, 749–749, https://doi.org/10.1017/S0016756808004627, 2007.
- Waddington, E. D., Bolzan, J. F., and Alley, R. B.: Potential for stratigraphic folding near ice-sheet centers, J. Glaciol., 47, 639–648, https://doi.org/10.3189/172756501781831756, 2001.
- Weertman, J.: Creep deformation of ice, Annual Review of Earth and Planetary Sciences, 11, 215–240, https://doi.org/10.1146/annurev.ea.11.050183.001243, 1983.

- Weikusat, I., Jansen, D., Binder, T., Eichler, J., Faria, S. H., Wilhelms, F., Kipfstuhl, S., Sheldon, S., Miller, H., Dahl-Jensen, D., and Kleiner, T.: Physical analysis of an Antarctic ice core towards an integration of micro- and macrodynamics of polar ice, Philos. Trans. R. Soc. A: Math., Phys. Eng. Sci., 375, 20150347, https://doi.org/10.1098/rsta.2015.0347, 2017.
- Weikusat, I., Westhoff, J., Kipfstuhl, S., and Jansen, D.: Visual stratigraphy of the EastGRIP ice core (14 m-2021 m depth, drilling period 2017-2019), PANGAEA [data set], https://doi.org/10.1594/PANGAEA.925014, 2020.
- Westhoff, J., Stoll, N., Franke, S., Weikusat, I., Bons, P., Kerch, J., Jansen, D., Kipfstuhl, S., and Dahl-Jensen, D.: A Stratigraphy Based Method for Reconstructing Ice Core Orientation, Annals of Glaciology, 62, 191–202, https://doi.org/10.1017/aog.2020.76, 2021.
- Wolovick, M. J., Creyts, T. T., Buck, W. R., and Bell, R. E.: Traveling slippery patches produce thickness-scale folds in ice sheets, Geophys. Res. Letts., 41, 8895–8901, https://doi.org/10.1002/2014GL062248, 2014.
- Zhang, Y., Sachau, T., Franke, S., Yang, H., Li, D., Weikusat, I., and Bons, P. D.: Formation Mechanisms of Large-Scale Folding in Greenland's Ice Sheet, Geophys. Res. Letts., 51, e2024GL109492, https://doi.org/10.1029/2024GL109492, 2024.